Determination of degradation modes of lithium-ion batteries considering aging-induced changes in the half-cell open-circuit potential curve of silicon–graphite

Julius Schmitt [a,*], Markus Schindler [a], Andreas Oberbauer [a], Andreas Jossen [a,b]

[a] Technical University of Munich, School of Engineering and Design, Department of Energy and Process Engineering, Chair for Electrical Energy Storage Technology, Arcisstraße 21, 80333 Munich, Germany
[b] Technical University of Munich, Munich School of Engineering, Lichtenbergstraße 4a, 85748 Garching, Germany

HIGHLIGHTS

- Aging-induced change in SiC OCP curve is analyzed using a blend electrode model.
- Aged full-cell OCV curves are reconstructed using measured aged SiC OCP curves.
- Full-cell OCV curves are reconstructed using simulated SiC OCP curves.
- Degradation modes are estimated with higher validity avoiding misinterpretations.
- Destruction-free estimation method for component degradation in SiC is presented.

ARTICLE INFO

ABSTRACT

The shape of the open-circuit potential (OCP) curve of silicon–graphite blend electrodes changes during cycle aging due to the faster degradation of the silicon in comparison to the graphite. In this study, the impact of these changes on the open-circuit voltage (OCV) curve of full-cells is investigated. Reconstructing the OCV curve of aged cells by shifting and linearly scaling pristine half-cell OCP curves is an established diagnostic method of determining the degradation modes occurring in lithium-ion cells. We reconstruct the full-cell OCV curves of cycle-aged commercial cells with silicon–graphite anodes using both pristine and aged silicon–graphite OCP curves. Lower estimates are obtained for the loss of anode active material and higher estimates for the loss of both cathode active material and lithium inventory, when aging-induced changes in the shape of the silicon–graphite OCP are considered. Aging-induced changes in the shape of silicon–graphite OCP curves are integrated in the diagnostic method by using a blend electrode OCP model. This not only improves the validity of the determined degradation modes, but also enables the non-destructive estimation of the anode capacity fraction provided by silicon, based on full-cell OCV measurements.

1. Introduction

The capacity and power that can be provided by a lithium-ion cell decreases during long-term operation [1–3] and storage [4–6]. A vast number of degradation mechanisms have been identified as possible causes of the decrease in cell performance during aging [7]. Most methods used to identify individual degradation mechanisms are complex and necessitate the destruction of the cell during post-mortem analysis, rendering them unusable for onboard application and also limiting their applicability in research. Therefore, rather than analyzing individual mechanisms, the degradation of lithium-ion cells is often analyzed in terms of degradation modes. Degradation modes are clusters of various degradation mechanisms that result in the same observable changes on the cell level [7,8].

Dubarry et al. established a model that describes aging-induced changes in the full-cell open-circuit voltage (OCV) curve, based on three main degradation modes: loss of active material of the anode (LAM_{an}), loss of active material of the cathode (LAM_{cat}), and loss of lithium inventory (LLI) [8]. The model enables degradation modes to be determined based on the cell voltage during low-current charging or discharging, by aligning the open-circuit potential (OCP) curves of both electrodes to the full-cell OCV curve until the difference between the OCP curves fits the measured full-cell OCV curve. Many different

Table 1
Nominal cycles during the cycling period and full-cell charging capacity of cells at different aging states.

Cycles	Q_{tot}/EFC	C_{full}/Ah	ΔC/%
0	9	3.40	0
50	54	3.35	1.5
100	101	3.30	2.9
400	361	3.01	11.6
450	410	3.06	10.0
500	444	2.99	11.9
550	486	2.91	14.3

variants of this diagnostic method have been developed and used in recent years [9–21]. The definition and number of observed degradation modes differs between the various studies, as does the model used to simulate the full-cell OCV curve.

The shape of the OCP curve of the individual electrodes is generally regarded to be invariant during battery aging in the models used for analyzing degradation modes based on the full-cell OCV. This means that the OCP curve of an aged electrode can be obtained by linear scaling of the OCP curve of a pristine electrode. Some recent studies consider changes in the shape of the electrode OCP curves. Lee et al. propose an algorithm for adapting the shape of the OCP curve of lithium nickel manganese cobalt oxide (NMC) cathodes during aging [21]. Jia et al. show that the OCV of aged cells can be reconstructed with higher accuracy if the OCP curves of aged electrodes are used [19]. Schindler et al. propose modeling non-uniform electrode degradation using state of charge (SOC) dependent scaling of the half-cell curves [16].

In a recent study [22], we showed that the shape of the OCP curve of NMC-811 does not change significantly when cycled in the full-cell configuration. In contrast, we detected aging-induced changes in the shape of the OCP curve of silicon–graphite. We interpret these changes as being the result of the faster degradation of silicon than graphite during cycling. This affects the relative capacity contribution of both components and, in turn, the shape of the OCP curve of the blend electrode [22]. Increased degradation of the silicon in silicon–graphite blend electrodes in comparison to the graphite has also been reported by other authors [23–26]. It is attributed to increased electric and ionic contact loss of the silicon due to its pronounced expansion and contraction during lithiation and delithiation [23] and morphological changes during cycling [27]. The influence of such changes in the relative capacity contribution of silicon and graphite on the full-cell OCV curve during aging has been described using a blend electrode model [28].

This study expands on our previous findings [22] and investigates the influence of aging-induced changes in the shape of the silicon–graphite OCP curve on the full-cell OCV curve. To our knowledge, this is the first study, in which silicon–graphite half-cell OCP curves measured for cells at a series of aging states are used to reconstruct the full-cell OCV curve at the corresponding aging state. We analyze how changes in the shape of the silicon–graphite OCP influence the degradation modes determined from full-cell OCV curves and propose an extension of the diagnostic method presented by Dubarry et al. [8] that considers changes in the silicon–graphite OCP curve by using the blend electrode model presented by Schmidt et al. [9]. This approach of using a synthetic half-cell OCP curve calculated from pristine pure silicon and graphite OCP curves for the reconstruction of measured aged full-cell OCV curves has, to our knowledge, not been presented in the literature before. It enables the anode capacity fraction provided by the silicon to be estimated based on full-cell OCV curves and half-cell OCP curves of pristine electrode components, without the need for opening up aged cells and performing measurements on aged electrode samples.

2. Experimental

The experimental procedure used for cycling and characterizing commercial full-cells and harvested electrode samples was reported on in our previous work [22]. For this reason, we only provide a summary of the experimental procedure here. For further details, the reader is referred to the original work [22].

This study investigates commercially available cells of the type INR18650-MJ1 (MJ1) made by LG Chem. The cell format is 18 650 and the nominal minimum capacity is 3.35 Ah. The anode active material of this cell consists of a blend of graphite in the shape of ellipsoidal flakes with an average diameter of 15 μm [29] and particles of silicon-based compounds (SiO_x where x is equal to 0, 1, or 2, etc.) that have the shape of sharp-edged shards with an average diameter of 3 μm [29]. Different values for the mass ratio of silicon inside the anode material of this cell type are reported in the literature ranging from 1 wt.% to 5 wt.% [26,29–31]. NMC-811 is used for the cathode active material [29,31]. Full-cell C-rates used in this work refer to a nominal capacity of 3.35 Ah. One equivalent full cycle (EFC) refers to a charge throughput of twice the nominal capacity, which is 6.7 Ah.

The cells were first characterized using a series of procedures that are internally standardized at our institute to determine the long-term evolution of cell characteristics of this type of commercial cell [1,32, 33]. A capacity checkup was then conducted comprising two constant current constant voltage (CCCV) cycles. The quasi-stationary OCV of the cells in the pristine state was then measured using low-current CCCV discharging and subsequent CCCV charging between 2.5 V and 4.2 V. The current rate during the constant current (CC) phases was C/30, and a cut-off current of C/1000 was used as the termination criterion for the constant voltage (CV) phase.

The cells were subsequently cycled for up to 550 cycles using CCCV charging and CC discharging at 25 °C. A current rate of C/2 was used for charging, while 1 C was used for discharging. The number of cycles after which the procedure was terminated differed for each cell so as to provoke different levels of degradation (see Table 1).

After the cycling, the quasi-stationary OCV of the aged cells was measured using the procedure described above, and the cells were finally discharged to 3 V using CCCV discharging. The cells were then opened up in an argon-filled glove box and samples from both electrodes were extracted. One cell was not cycled but discharged directly and opened up after characterization to measure the quasi-stationary OCP in the pristine state. The electrode samples were weighed using an analytical scale (Quintix 224-1S, Sartorius Mechatronics), and the quasi-stationary OCP was determined using coin-cell measurements with lithium metal foil as the counter electrode. A low current rate of approximately C/90 was used for the measurement. Details of the coin-cell measurement procedure can be found in Ref. [22].

In addition to the experiments described in Ref. [22], the quasi-stationary OCP of graphite was also measured in this study. Round samples with a diameter of 14 mm were punched out of a sheet of commercially available natural graphite with a mass loading of 13.0 mg cm^{-2}. The sheet was made up of a copper conductor with a graphite coating on both sides. The coating was removed on one side before the samples were obtained. Coin-cells containing a graphite sample and a piece of lithium metal foil as a counter electrode were subsequently constructed. The coin-cells were produced in the same way as described in Ref. [22]. Five formation cycles were applied as follows: CCCV lithiation with a current rate of C/10, a cut-off voltage of 0.01 V, and a cut-off current of C/50 followed by CC delithiation with a current rate of C/10 and a cut-off voltage of 1.7 V. There was a one-hour rest period between each lithiation and delithiation step. The C-rates for these coin-cells refer to a nominal capacity of 5.43 mAh.

The graphite was subsequently CCCV delithiated using a current rate of C/10, a cut-off voltage of 1.7 V, and a cut-off current of C/100. After a rest time of 100 s, the graphite was lithiated at a current rate of C/100 until a cut-off voltage of 0.01 V to measure the quasi-stationary OCP during lithiation. Both formation and OCP measurements were conducted at 25 °C inside an ESPEC LU-123 climatic chamber and using a BaSyTec CTS battery test system.

3. Model and methodology

3.1. Full-cell open-circuit voltage model and degradation diagnosis

The model and method for quantifying degradation modes presented in the following is based on the concept presented by Dubarry et al. [8]. The OCV of a full-cell U_{full} at a certain full-cell SOC x_{full} is calculated as:

$$U_{full}(x_{full}) = U_{cat}(x_{cat}) - U_{an}(x_{an}), \qquad (1)$$

where $U_{cat}(x_{cat})$ is the cathode OCP at this full-cell SOC and $U_{an}(x_{an})$ is the anode OCP at this full-cell SOC. The measured potential curves for the anode $U_{an}(x_{an})$ and cathode $U_{cat}(x_{cat})$ are defined as functions of the electrode SOC x_{an} or x_{cat}. The electrode SOC of the anode x_{an} is defined as the amount of lithium inserted into the anode divided by the total amount of lithium inserted into the anode during a lithiation from 1.7 V to 0.01 V. Its value is therefore between 0 and 1, where 1 corresponds to the lithiated state. The electrode SOC of the cathode x_{cat} is defined as the amount of lithium extracted from the cathode divided by the total amount of lithium extracted from the cathode during a delithiation from 3.0 V to 4.3 V. Its value is therefore between 0 and 1, where 1 corresponds to the delithiated state at $U_{cat} = 4.3$ V.

The half-cell voltage limits are chosen as suggested in Ref. [31] to cover at least the lithiation window in which the electrodes are operated in the full-cell configuration throughout the aging. In principle, wider operating limits could be chosen for the half-cells, but we assume for the definition of electrode SOC and capacity that the half-cells should only be operated in the respective voltage windows due to the following considerations: Further delithiation of silicon–graphite would not lead to a significant capacity increase, as it already reaches a virtually fully delithiated state at 1.7 V vs. Li/Li⁺ [34]. Any further lithiation would lead to a high risk of lithium plating. The NMC-811 is virtually fully lithiated at 3.0 V vs. Li/Li⁺ [35,36] and any further delithiation above 4.3 V vs. Li/Li⁺ would lead to increased degradation due to the formation of a surface rock-salt type layer [37].

Calculating the full-cell OCV curve requires a description of both electrode potentials as a function of the full-cell SOC. This can be obtained by aligning the half-cell curves with the full-cell curve as shown in Fig. 1(a). In this figure, both normalized half-cell curves are linearly scaled and shifted with respect to the SOC-axis in order to fit the full-cell curve. This linear scaling and shifting of the electrode OCP curves resembles a transformation of the electrode SOC into the corresponding full-cell SOC. For the anode SOC, this transformation is defined as:

$$x_{full} = \alpha_{an} \cdot x_{an} + \beta_{an}, \qquad (2)$$

where α_{an} is the factor by which the anode OCP curve is scaled to fit the full-cell curve and β_{an} is the value by which the anode curve is shifted towards higher full-cell SOC to fit the full-cell curve. α_{an} can be interpreted as the factor by which the anode capacity is oversized in comparison to the full-cell capacity. The cathode SOC in the coordinate system of the full-cell is described by:

$$x_{full} = \alpha_{cat} \cdot x_{cat} + \beta_{cat}, \qquad (3)$$

where α_{cat} is the linear scaling factor and β_{cat} is the shift of the cathode OCP curve towards higher SOC. In this model, the point of origin for the scaling of the half-cell OCP is always 0 % electrode SOC, which corresponds to the delithiated state for the anode and the lithiated state for the cathode. As both electrode curves need to have their origin at or below 0 % full-cell SOC, β_{an} and β_{cat} are always negative, which means that the curves are left-shifted in the full-cell coordinate system. By rearranging Eqs. (2) and (3), the respective electrode SOC can be calculated from the full-cell SOC:

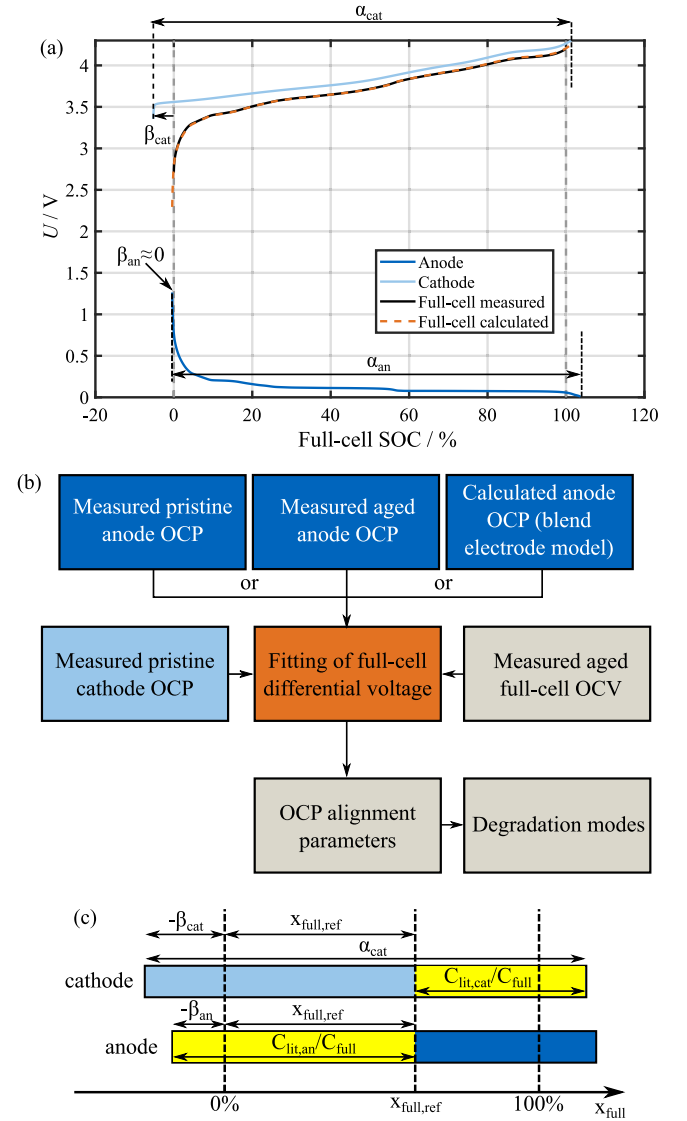$$x_{an} = (x_{full} - \beta_{an})/\alpha_{an}, \qquad (4)$$

Fig. 1. (a) Reconstruction of a pristine full-cell OCV curve by linear scaling and shifting of pristine half-cell OCP curves. (b) Flowchart describing the method applied in this study for analyzing the impact of changes in the anode half-cell OCP curve on the determination of degradation modes. (c) Schematic representation of the definition of the lithium inventory.

$$x_{cat} = (x_{full} - \beta_{cat})/\alpha_{cat}. \qquad (5)$$

Substituting Eqs. (4) and (5) into Eq. (1) yields a description of the full-cell voltage as a function of full-cell SOC:

$$U_{full}(x_{full}) = U_{cat}((x_{full} - \beta_{cat})/\alpha_{cat}) - U_{an}((x_{full} - \beta_{an})/\alpha_{an}). \qquad (6)$$

This model enables full-cell OCV curves at different aging states to be described based on measured half-cell curves by adjusting the alignment parameters (α_{an}, α_{cat}, β_{an} and β_{cat}) until the reconstructed full-cell curve fits the measured curve. The alignment parameters can be used to determine the remaining capacity of the individual electrodes, the remaining lithium inventory in the electrodes, and the cell balancing.

The degradation modes are calculated based on the best fit for the alignment parameters. The anode capacity C_{an} at a certain aging state is calculated as the remaining full-cell capacity C_{full} multiplied by the anode scaling factor α_{an} at this aging state. The relative LAM_{an} at a certain aging state is then defined as:

$$LAM_{an} = \frac{C_{an,ini} - C_{an}}{C_{an,ini}}, \qquad (7)$$

where $C_{\text{an,ini}}$ is the anode capacity in the pristine state. The relative LAM_{cat} is defined in a similar way. The lithium inventory C_{lit} is the lithium available for delithiation in both electrodes [20] starting from an arbitrary reference SOC $x_{\text{full,ref}}$ within the voltage limits of the full-cell. The lithium inventory in the electrodes is calculated by:

$$C_{\text{lit}} = C_{\text{lit,an}}(x_{\text{full,ref}}) + C_{\text{lit,cat}}(x_{\text{full,ref}}), \qquad (8)$$

where $C_{\text{lit,an}}(x_{\text{full,ref}})$ is the capacity of the available lithium in the anode and $C_{\text{lit,cat}}(x_{\text{full,ref}})$ the capacity of the available lithium in the cathode when the full-cell is at the reference SOC $x_{\text{full,ref}}$. The term available lithium refers to the amount that can be potentially delithiated until the half-cell upper cut-off voltage of the respective electrode is reached. Regarding the capacity of the available lithium in the anode, the following applies:

$$C_{\text{lit,an}}(x_{\text{full,ref}}) = C_{\text{full}} \cdot (x_{\text{full,ref}} - \beta_{\text{an}}), \qquad (9)$$

as the capacity of the available lithium in the anode is $C_{\text{full}} \cdot x_{\text{full,ref}}$ plus the portion of the anode capacity below 0 % full-cell SOC, which is equal to $C_{\text{full}} \cdot (-\beta_{\text{an}})$. The negative sign is necessary, as β_{an} is defined as negative for a left-shifted anode curve. The capacity of the available lithium in the cathode is given by:

$$C_{\text{lit,cat}}(x_{\text{full,ref}}) = C_{\text{full}} \cdot (\alpha_{\text{cat}} - x_{\text{full,ref}} + \beta_{\text{cat}}), \qquad (10)$$

as it is the complete cathode capacity ($C_{\text{full}} \cdot \alpha_{\text{cat}}$) minus the delithiated part below $x_{\text{full,ref}}$. The concept of this definition for C_{lit} is shown as a schematic in Fig. 1(c). Substituting Eqs. (9) and (10) into Eq. (8) yields:

$$C_{\text{lit}} = [(x_{\text{full,ref}} - \beta_{\text{an}}) + (\alpha_{\text{cat}} - x_{\text{full,ref}} + \beta_{\text{cat}})] \cdot C_{\text{full}}. \qquad (11)$$

It should be noted that $x_{\text{full,ref}}$ cancels out in Eq. (11), as the lithium inventory does not depend on the chosen reference SOC. The relative LLI is defined as

$$\text{LLI} = \frac{C_{\text{lit,ini}} - C_{\text{lit}}}{C_{\text{lit,ini}}}. \qquad (12)$$

The following algorithm is used for the alignment of half-cell and full-cell curves. Both half-cell and full-cell curves are normalized, i.e., the measured charge throughput during charging of the full-cell, lithiation of the anode, or delithiation of the cathode, is divided by the charge throughput at the end of the procedure. A full-cell OCV curve is then calculated using Eq. (6) with an initial estimate of the alignment parameters. Next, the differential voltage (DV):

$$\left.\frac{dU}{dQ}\right|_{x_{\text{full}}} = \frac{U_{\text{full}}(x_{\text{full}} + \Delta x) - U_{\text{full}}(x_{\text{full}})}{\Delta x} \qquad (13)$$

is calculated at 2001 equally spaced interpolation points between $x_{\text{full}} = 0$ and $x_{\text{full}} = 1$ for both the calculated and the measured full-cell OCV curve. Interpolating at this number of points, in our case, yields a sufficiently high resolution of the DV curve in the SOC dimension while the optimization can be executed in an appropriate time. Δx is a small fraction (0.2 %) of the SOC range for which the OCV curve is linearly approximated to calculate the local differential voltage. Then, the difference between the DV of the calculated and the measured OCV is evaluated at each interpolation point to obtain a measure of the fitting of both curves. The *lsqnonlin* function using the trust-region-reflective algorithm implemented in MATLAB® is used to minimize the sum of squared differences between the DV curves by varying the alignment parameters. The difference between the DV curves is used instead of the absolute OCV difference as an objective function for optimization, in order to align the features of the DV curves that represent the phases and phase transitions of the active materials and to minimize the influence of absolute offsets of the OCV curves. The difference between the DV curves at the edges of the full-cell SOC range (1 % at each side) is excluded to avoid the optimization being dominated by the steep slope of the OCV curves near the edges.

The influence of aging-induced changes in the shape of the anode OCP curve, i.e., a change in the function $U_{\text{an}}(x_{\text{an}})$, is investigated as follows: The quasi-stationary full-cell OCV, measured during low-current charging of the cells at different aging states just before they are opened up, is fitted with half-cell OCP curves according to the method described above. In the case of the cathode OCP, the half-cell curve measured with material extracted from the pristine full-cell is always used, because the shape of the curve does not change significantly during cycle aging [22]. Three different anode curves are used: the curve measured for material extracted from the pristine full-cell, the curve measured for the aged anode material extracted from the respective cell following the full-cell OCV measurement, and a synthetic curve calculated using a blend electrode model as described in Section 3.2. The measured OCP curves are averaged from multiple samples [22] and smoothed with a moving average filter before fitting.

A set of alignment parameters is thus obtained for each investigated aging state and for all three types of anode OCP curves. Finally, the degradation modes are calculated based on the different sets of alignment parameters. A schematic of the approach used in this study is shown in Fig. 1(b).

3.2. Silicon–graphite blend open-circuit potential model and determination of component degradation

We model the OCP curve of the silicon–graphite blend electrode using the following model, which was described by Schmidt et al. for a generic blend electrode [9]. The fraction of the capacity that can be inserted into a component of the silicon–graphite blend during lithiation until a potential U is reached is denoted as $Q_{\text{Si}}(U)$ for the silicon and $Q_{\text{G}}(U)$ for the graphite. The fraction of the blend anode capacity that is lithiated at this voltage is then given by:

$$Q_{\text{blend}}(U) = \gamma_{\text{Si}} \cdot Q_{\text{Si}}(U) + (1 - \gamma_{\text{Si}}) \cdot Q_{\text{G}}(U), \qquad (14)$$

where γ_{Si} is the fraction of the total anode capacity provided by the silicon. At the lower cut-off voltage U_{min}, both $Q_{\text{Si}}(U)$ and $Q_{\text{G}}(U)$ are equal to one by definition, and therefore $Q_{\text{blend}}(U)$ is also one. $Q_{\text{Si}}(U)$ and $Q_{\text{G}}(U)$ are obtained by taking the inverse of the OCP curve of the respective component as a function of normalized charge. The OCP of the blend anode as a function of normalized charge or electrode SOC Q_{blend} can then be obtained from:

$$U_{\text{OCV,blend}}(Q_{\text{blend}}) = f^{-1}(Q_{\text{blend}}(U)). \qquad (15)$$

The shape of $U_{\text{OCV,blend}}(Q_{\text{blend}})$ is affected by the value of γ_{Si}. The blend OCP curve is similar to that of graphite for small values of γ_{Si} and similar to that of silicon for large values of γ_{Si}. Fig. 2(a) shows OCP curves for graphite and silicon. The graphite curve is measured as described in the experimental section. Small local minima (<1 mV) in the voltage curve occurring during lithiation, which are most probably measurement artifacts, are removed to enable inversion of the curve. The lithiation curve of pure silicon is taken from Li et al. [38].

This model is used to determine the capacity fraction of the silicon component of a silicon–graphite anode, by constructing blend OCP curves for various values of γ_{Si} and minimizing the difference between the DV curves of the calculated and measured OCP curves. The optimization procedure is the same as the one used for fitting the full-cell OCV curves with half-cell OCP curves. Again, 1 % of the electrode SOC range are excluded at both edges of the voltage window during the optimization.

We also use synthetic OCP curves calculated with the blend electrode model to reconstruct measured full-cell OCV curves. To do this, a silicon–graphite OCP curve is first calculated using the blend electrode model. Then, the full-cell OCV curve is reconstructed by aligning both the synthetic anode OCP and the pristine cathode OCP. The silicon capacity fraction γ_{Si} used to calculate the anode OCP is then optimized along with the four alignment parameters.

If the gravimetric specific capacities of both components are known, an estimate for the mass fraction of the pristine anode that consists of silicon can be calculated, based on γ_{Si}. The silicon mass fraction can be obtained as a function of γ_{Si} by:

$$\frac{m_{Si}}{M_{blend}} = \frac{\gamma_{Si} \cdot c_G}{c_{Si} - \gamma_{Si} \cdot (c_{Si} - c_G)}, \qquad (16)$$

where m_{Si} is the silicon mass, M_{blend} the total mass of the active blend material, c_{Si} the gravimetric specific capacity of silicon, and c_G the gravimetric specific capacity of graphite. The derivation of Eq. (16) can be found in the Appendix.

4. Results and discussion

As reported in our previous work [22], the investigated cells are at different aging states following cycling periods of varying duration. Table 1 lists the total charge throughput Q_{tot}, i.e., the number of equivalent full-cycles applied to the cells until the quasi-stationary OCV measurement prior to cell opening. In this study, the charge throughput during low-current charging after cycling and prior to cell opening is taken as the value of the remaining full-cell capacity C_{full}. Table 1 also lists the remaining full-cell capacities of the individual cells along with the relative capacity losses ΔC. In this section, we will analyze the degradation modes occurring during cell cycling.

4.1. Changes in the silicon–graphite open-circuit potential curve

To illustrate the calculation of a silicon–graphite OCP curve using the blend electrode model, Fig. 2(a) shows the measured and calculated OCP curves of a pristine electrode using $\gamma_{Si} = 9.52\%$, which is obtained by optimization. The calculated curve fits the measured curve well. The right-shift of the graphite features in comparison to the pure graphite curve can be simulated particularly well with the model. The root-mean-square error (RMSE) between the measured and the calculated OCP curve is 6.6 mV.

In our previous work [22], we show that the shape of the OCP curve of the silicon–graphite used in the investigated cell type changes during cycle aging. The most prominent changes are a left-shift of both the graphite and silicon DV peaks towards a lower electrode SOC. This change is most probably caused by a decrease in the fraction of the electrode capacity provided by the silicon. The blend electrode model is capable of simulating OCP curves of electrodes with varying capacity contributions of the components and is therefore used here to describe the changes in the shape of the silicon–graphite OCP curves. The silicon–graphite OCP curves measured at different aging states are fitted using the model. As an example, the measured and calculated OCP curves of both the pristine silicon–graphite and the silicon–graphite cycled for 488 EFC in the full-cell configuration are shown in Fig. 2(b). The model is able to capture the aging-induced changes in the curve shape. The model captures the reduced charge inserted between 0.3 V and 0.2 V due to reduced silicon capacity and the shift of voltage slopes associated with graphite stages 4L to 2L towards lower SOC particularly. The RMSE between the calculated and the measured OCP curve is below 6.9 mV for all aging states, which shows that the model is suitable for fitting OCP curves of aged cells. This finding has two implications: First, it supports the theory that the change in the silicon–graphite OCP is caused by a faster capacity decrease of the silicon compared to the graphite [22]. Second, fitting aged OCP curves of silicon–graphite with the blend electrode model serves as a diagnostic tool for obtaining an estimate of the capacity fraction provided by both electrode components during cell aging.

Fig. 2(c) shows the fitting results of the relative capacity contribution of silicon γ_{Si} for the different aging states. There is a clear trend towards a lower capacity contribution of silicon as aging progresses. Predominant degradation of the silicon in silicon–graphite has also been reported in the literature [23–25,39]. The deviation of single data
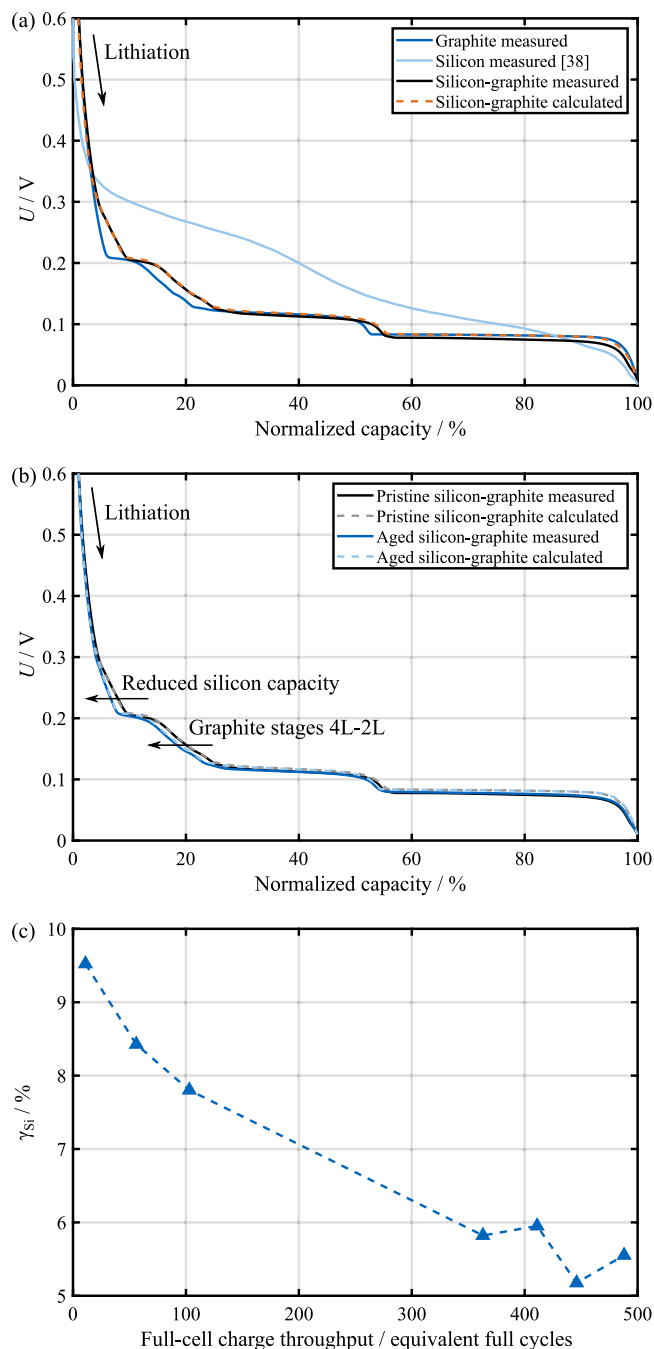

Fig. 2. (a) Reconstruction of the measured pristine silicon–graphite OCP curve based on the normalized lithiation curves of the electrode components using the blend electrode model. The lithiation curve of silicon is obtained from Ref. [38]. (b) Measurement and model calculation of a pristine and a cycle aged (488 EFC) silicon–graphite electrode. (c) Fraction of the silicon–graphite electrode capacity provided by silicon determined by fitting silicon–graphite half-cell curves at different aging states with the blend electrode model.

points from this trend is probably due to intrinsic cell variations, leading to differences in the aging behavior of the individual cells [1,33]. The fraction of the electrode capacity provided by the silicon for the electrode to which the most cycles (488 EFC) are applied is estimated at 5.55%, which is only about 58% of the initial value.

Using the theoretical values of the gravimetric specific capacities $c_{Si} = 3579$ mAh g^{-1} [25,38] and $c_G = 372$ mAh g^{-1} [40], in Eq. (16), the mass fraction of electrochemically active silicon as part of the silicon–graphite blend is determined to be 1.08%. If it is assumed

that 5 wt.% of the anode material is made up of binder and carbon black, electrochemically active silicon should comprise 1.03 % of the total anode mass for pristine electrodes of this type. The total amount of silicon in the anode is probably higher, as higher values of the mass fraction of silicon have been reported in the literature for this cell type, but part of the silicon might be electrochemically inactive. Approximately 3.5 wt.% silicon was determined by inductively coupled plasma-optical emission spectroscopy (ICP-OES) [31], approximately 4.5 wt.% using energy-dispersive X-ray spectroscopy (EDS) [26] and approximately 3–4 wt.% using X-ray computed tomography (CT) [29]. It should also be noted that the precise composition of this commercial cell type has changed in recent years and the relative silicon content of the anode is lower for cells that were produced later, due to a change in the composition used by the manufacturer [32]. Therefore, the cells investigated in this study probably also contain less total silicon than those whose silicon content was reported in Refs. [26,29,31], even though they are of the same type.

To check the plausibility of our estimate of the electrochemically active silicon mass, we will now compare the calculated and measured absolute capacities of the pristine coin-cell samples. The average mass of the anode samples, including current collectors, is 35.9 mg. Subtracting an estimated mass for the current collector of 15.2 mg [31] yields an average electrode mass of 20.8 mg corresponding to a mass loading of 13.5 mg cm^{-2}. We assume that 5 % of the electrode mass comprises inactive components and 3.5 % [29,31] of the electrode mass consists of silicon, but only 1.03 % of the electrode mass is electrochemically active silicon and the remaining part is electrochemically inactive. The remaining 91.5 wt.% of the electrode mass is assumed to be graphite. Using these estimates and the theoretical gravimetric specific capacities, the absolute coin-cell capacity is calculated as 7.84 mAh. The average measured capacity during lithiation of the pristine silicon–graphite samples is 7.40 mAh. The calculated and measured capacities thus differ by less than 6 %, which leads us to the conclusion that our estimate of the capacity fraction provided by the silicon is plausible. If the entire 3.5 wt.% silicon were electrochemically active, the calculated coin-cell capacity would be 9.55 mAh, which clearly exceeds the measured value of 7.40 mAh. Our conclusion is therefore that a significant part of the silicon in the anode is electrochemically inactive which explains the discrepancy between our estimate regarding the silicon mass fraction and the results for the total silicon mass fraction provided in the literature [26,29,31]. Besides, a silicon capacity fraction of 10 % was also reported for a commercial silicon–graphite electrode with 3–4 wt.% silicon in Ref. [28]. The diagnostic method used to determine the capacity fraction provided by the silicon presented in our study might be an even better indicator of the practically usable silicon capacity than estimations based on the measured total silicon mass fraction, because the method only considers electrochemically active silicon, which might only be a fraction of the present silicon and also might change during cell aging.

4.2. Changes in the full-cell open-circuit voltage curve

Fig. 3(a) displays the quasi-stationary OCV during low-current charging for cells that have undergone different numbers of cycles. As a general trend, the absolute voltage at the same SOC increases with cycling. This is probably due to LLI leading to a shift in cell balancing such that the cathode is in a more delithiated state at the same full-cell SOC during full-cell charging [23]. In addition, the positions of the features of the OCV curve change, as analyzed on the basis of the DV curves. In Fig. 3(b), the normalized DV is plotted against the SOC. The peaks in the DV plot correspond to lithiation phases of the anode or the cathode. The minima correspond to phase transition regimes where two lithiation phases coexist. In Fig. 3(b), the peaks are associated with lithiation phases based on Refs. [4,37,41].

Changes in the shape of the OCV curve are evident during cycle aging. The peaks of the DV curve are at a lower SOC for aged cells,

which means that the lithiation phases are reached earlier on in the charging process. There are two changes in the curve features that can be attributed to the cathode: The broad central peak between approximately 50 % and 60 % SOC corresponding to the monoclinic M-phase of NMC-811 [37] shifts to the left during cycling. This peak is not clearly visible for the pristine and mildly aged cells, as it is superimposed with the stage 2 peak of the graphite. Due to the left-shift, this peak becomes discernible for cells cycled for ≥361 EFC. The peak around 80 % SOC corresponding to the hexagonal H2-phase of NMC-811 [37] also shifts to the left during cycling. Both of these peak shifts are probably due to a change in the balancing between the two electrodes. As cyclable lithium is lost, the cathode becomes more delithiated during charging of the full-cell. The cathode half-cell curve therefore shifts to the left in comparison to the anode half-cell curve [16]. For this cell type, the anode is always limiting at 0 % full-cell SOC, as will be shown in Section 4.3. Therefore, this relative shift of the cathode OCP curve results in a left-shift of the cathode peaks in the full-cell DV curve.

In addition to the changes related to the cathode, there are also changes that can be attributed to the anode. The peaks corresponding to the partly lithiated graphite stages between 4L and 2L around 20 % SOC [41] shift to a lower SOC during aging. The peaks below 10 % SOC corresponding to silicon phases [4] are also located at a lower SOC for the cells that have been cycled for a longer period. There are two possible explanations for this observation: The traditional explanation, neglecting changes in the shape of the electrode OCP, would be that there is a higher relative loss of anode active material compared to the loss of cathode active material. This corresponds to a compression of the anode curve in the model. As the anode is limiting at 0 % SOC, compression of the anode OCP curve leads to a left-shift of the anode features in the full-cell OCV. But taking into account the results from our analysis on the electrode level, this shift of silicon and graphite peaks in the full-cell DV curve could also be caused by the changes in the shape of the anode half-cell OCP curve due to silicon degradation being faster than graphite degradation. As both effects would lead to the same results with regard to the full-cell OCV, the left-shift of the anode peaks in the full-cell DV can be misinterpreted as resulting solely from an overall anode active material loss. In fact, at least some of the left-shift of the anode peaks is most likely due to changes in the silicon–graphite half-cell curve caused by the faster degradation of silicon.

The central peak corresponding to stage 2 graphite exhibits some variation and decreases in height during aging, but there is no clear trend in its position. The decrease in the height of this peak is probably caused by an increase in the inhomogeneity of the anode [42–44].

4.3. Reconstruction of full-cell open-circuit voltage curves

The aging-induced changes in the quasi-stationary OCV curve during full-cell charging are analyzed quantitatively using the OCV model and the fitting procedure described in Section 3.1. In order to investigate the influence of changes in the shape of the silicon–graphite OCP during aging, the full-cell OCV curves are reconstructed using the pristine anode OCP curve, the aged anode OCP curve, i.e., the anode OCP measured at the same aging state as the full-cell OCV, and an OCP curve calculated using the blend electrode OCP model. As an example, the reconstruction of the OCV curve of the cell cycled for 486 EFC is shown in Fig. 4. The different interpretations of the changes in anode features in the full-cell OCV, depending on whether changes in anode half-cell OCP are considered, are visible here. In Fig. 4(a), the pristine anode half-cell curve is used to reconstruct the full-cell curve. The anode features in the full-cell curve, in particular the voltage slope associated with the 4L to 2L stages of graphite, are shifted to the left with respect to the pristine full-cell OCV. To obtain this left-shift in the reconstructed curve, the anode curve is compressed. This compression is interpreted as a loss of anode active material. Consequently, at 100 %
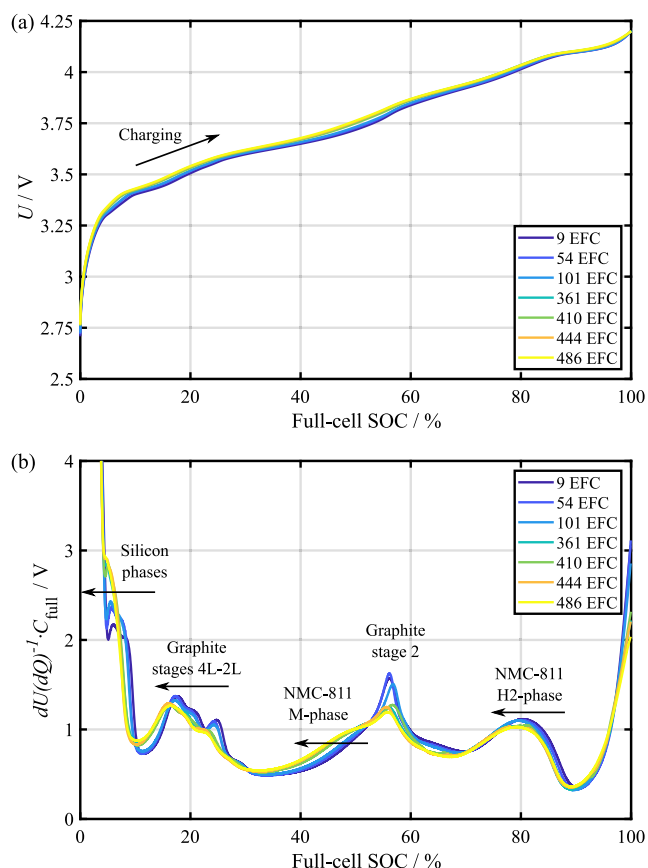
Fig. 3. (a) Quasi-stationary OCV curve of full-cells at different aging states during low-current (C/30) charging. (b) Normalized differential voltage of cells at different aging states during low-current charging.

full-cell SOC, the anode potential has already left the voltage plateau corresponding to the transition between graphite stage 2 and 1, and the anode potential is a limiting factor for reaching the upper full-cell cut-off voltage at the end of charging. In Fig. 4(b), the same aged full-cell OCV is reconstructed using the aged anode half-cell curve. This curve already exhibits a left-shift of the features related to anode lithiation phases on the half-cell level. Therefore, the anode curve is compressed less during the reconstruction of the full-cell curve. The same applies to the reconstruction of the full-cell curve using an anode curve simulated with the blend electrode OCP model shown in Fig. 4(c): Here, the left-shift of the anode features in the full-cell OCV is partly realized at the half-cell level by reducing the capacity contribution of silicon, and less compression of the whole anode curve is required compared to using the pristine anode curve. If changes in the half-cell OCP are considered, the anode is not identified as limiting at the end of charge, as the anode potential at 100 % full-cell SOC is still within the voltage plateau.

Fig. 5 shows the RMSE between the measured and the calculated full-cell OCV curve at different aging states for the three types of anode OCP curves. There is a general trend of increase in the RMSE with cell cycling. This might be due to an increase in electrode inhomogeneity during cycle aging [43,44], which also affects the OCV curve and is not considered in the model. Still, as the RMSE is always below 12 mV, a good agreement between the measured and the constructed curve is obtained for all three types of anode curves and at all aging states. Therefore, aging-related changes in the full-cell OCV curve can be accurately described with the model regardless of whether changes in the anode half-cell OCP are considered. But while having a small impact on fit accuracy, the consideration of changes in the half-cell OCP shape influences the quantitative results for the alignment parameters and therefore the interpretation of the changes in the full-cell OCV.
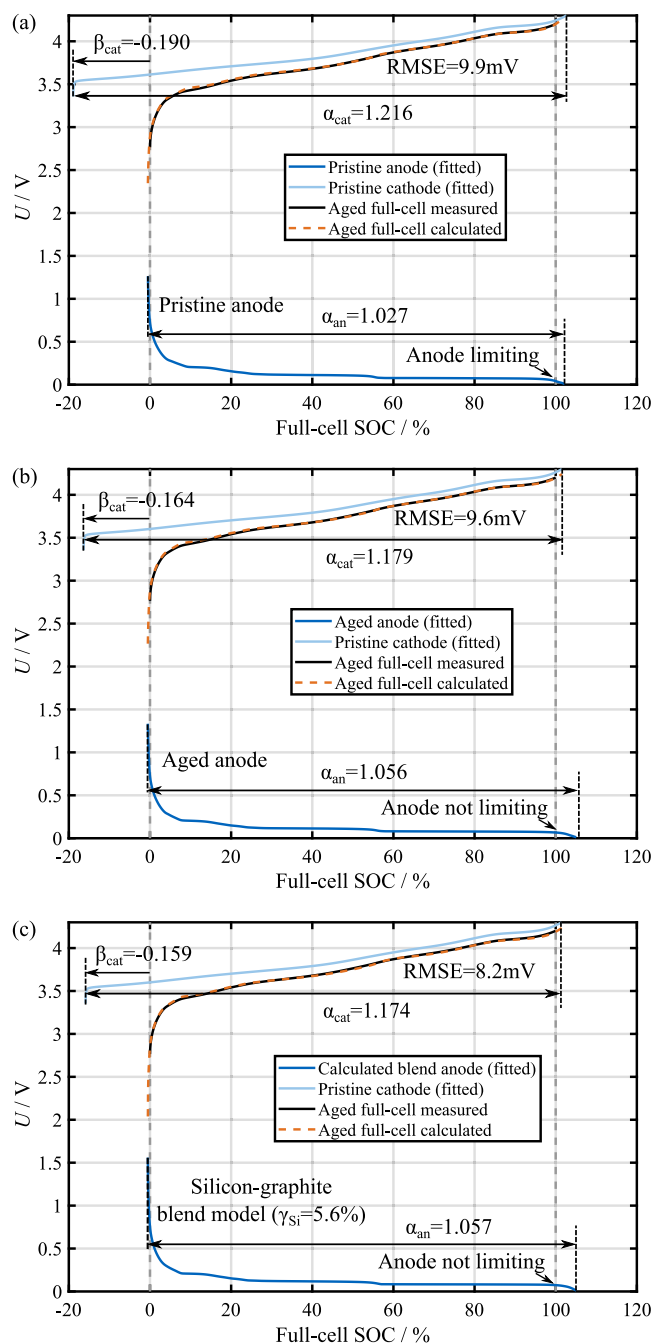

Fig. 4. Reconstruction of the quasi-stationary OCV during charging of a full-cell cycled for 486 EFC using (a) the anode half-cell curve of the pristine material, (b) the anode half-cell curve of the aged material, and (c) a synthetic anode OCP curve representing the half-cell curve of aged material calculated with the blend electrode model.

Fig. 6 contains plots of the four alignment parameters obtained at different aging states. The results are shown for all three types of anode curves. The progression of the anode scaling factor α_{an} is shown in Fig. 6(a). In the pristine state, the anode capacity is approximately 4 % larger than the full-cell capacity. An almost complete use of the anode has also been reported in the literature for this cell type [31]. Different trends for the progression of α_{an} are found, depending on whether changes in the anode half-cell OCP are considered. If the pristine anode OCP is used to reconstruct the aged full-cell OCV curves, there is a decreasing trend in α_{an} during aging. As discussed above, the left-shift of the anode features in the full-cell OCV curve is obtained by compressing the anode curve when the pristine anode OCP is used.
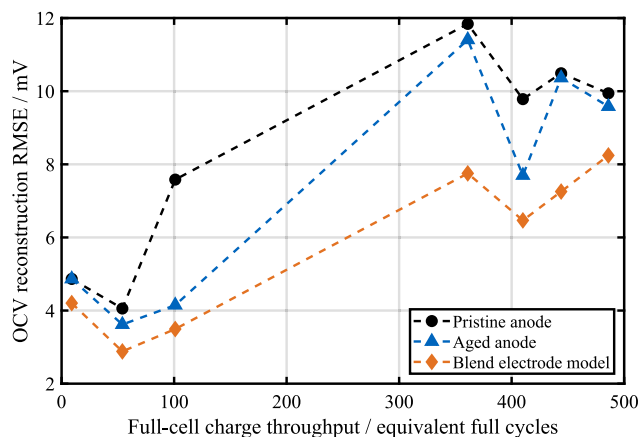
Fig. 5. Root-mean-square error for the reconstruction of the full-cell OCV at different aging states. The RMSE is plotted for using the pristine anode OCP, the aged anode OCP at a certain aging state, and synthetic OCP curves calculated with the blend electrode model.

A different result is obtained when changes in the anode half-cell OCP are considered: Regardless of whether the aged anode half-cell curves or the OCP curves calculated with the blend electrode model are used, α_{an} tends to increase during aging. However, this does not mean that there is an increase in absolute anode capacity. Rather, it should be interpreted such that less of the anode capacity is used within the voltage limits of the full-cell due to LLI.

The results of the anode offset β_{an} during aging are plotted in Fig. 6(b). The anode offset is close to zero ($|\beta_{an}| < 0.6\%$) throughout aging and for all types of anode curves. This means that the anode is always limiting the usable full-cell capacity at the lower cut-off voltage. There are small deviations (<0.12 percentage points) between the values of β_{an} obtained with the different types of anode curves, but these are probably due to the fitting and have no physical significance.

Fig. 6(c) shows plots of the progression of the cathode scaling factor α_{cat} during aging. For the pristine cell, the cathode capacity within the half-cell voltage limits is approximately 7% larger than the full-cell capacity. Similar results have previously been reported for this cell type [31]. The cathode scaling factor increases during cycling, which means that a smaller fraction of the cathode capacity is used with ongoing aging, probably caused by LLI. The values of α_{cat} obtained for the heavily aged cells (≥ 361 EFC) are more than 2 percentage points smaller if changes in the anode half-cell curve are considered in the reconstruction process.

The cathode offset β_{cat} at different aging states is shown in Fig. 6(d). The cathode offset is estimated to be approximately -5% for the pristine cell, which means that the cathode is not fully lithiated at the lower cut-off voltage of the full-cell. During aging, β_{cat} decreases further, corresponding to a left-shift of the cathode OCP curve. A relative left-shift of the cathode curve corresponds to LLI leading to a change in the balancing between the electrodes [16]. The decrease in β_{cat} is found to be smaller where changes in the shape of the anode OCP are considered.

4.4. Estimation of the silicon capacity based on full-cell open-circuit voltage curves

In Section 4.3 the influence of changes in the shape of the silicon–graphite OCP curve on the full-cell OCV curve during aging is analyzed by using measured aged silicon–graphite OCP curves and synthetic silicon–graphite OCP curves calculated with the blend electrode model to reconstruct aged full-cell OCV curves. While the first approach allows the impact of changes in the half-cell OCP on the degradation modes observable in the full-cell OCV curves to be analyzed on the basis

of experimental results, the latter approach is particularly suitable as a diagnostic method in research and applications as it requires less experimental effort. The measurement of aged half-cell OCP curves is not necessary with this procedure. Instead, the blend anode OCP curve is calculated based on the OCP curves of pristine pure graphite and pristine pure silicon. The anode capacity fraction provided by silicon γ_{Si} is obtained by optimization, i.e., variation of γ_{Si} and the four alignment parameters to minimize the difference between the DV of the measured and that of the reconstructed full-cell OCV. Using this procedure enhances the validity of the results of the degradation modes in comparison to using the pristine silicon–graphite curve for the reconstruction of the full-cell OCV. It also enables the capacity fraction of the anode provided by the silicon to be estimated, without necessitating the measurement of the half-cell OCP curves of aged cells.

The results obtained for the anode capacity fraction provided by silicon are shown in Fig. 7. The results we obtain by reconstructing the aged full-cell OCV curves are similar to those we obtain for the reconstruction of the aged half-cell curves presented in Section 4.1. Both sets of values are shown in Fig. 7. The difference between the estimation based on full-cell curves and the one based on half-cell curves is below 0.8 percentage points for all aging states. The results for γ_{Si} obtained by reconstructing the full-cell curves are slightly higher than those obtained by fitting the half-cell curves. Like the results based on half-cell curves, γ_{Si} determined from full-cell curves tends to decrease during aging. The anode capacity fraction provided by silicon is estimated at 10.3% for the pristine cell and 5.6% for the cell cycled for 486 EFC. Using Eq. (16) and assuming the theoretical gravimetric specific capacities for silicon and graphite, the silicon mass fraction of the pristine anode material is estimated at 1.1%.

The method we propose here may be useful for determining changes in the component balancing of composite electrodes. In addition to being non-destructive and easy to execute, the method has further possible advantages: Unlike methods that quantify total silicon mass such as ICP-OES [31] or EDS [26], this method only determines the capacity of the electrochemically active part of the silicon. In an application context, this quantity might be even more relevant than the total silicon mass. It also enables the degradation of the silicon to be analyzed, which is not possible with methods that determine total silicon mass, as the quantity does not change during aging [26], even though the usable capacity of the silicon decreases.

4.5. Determination of degradation modes

The degradation modes occurring during the cycling are calculated using the results of the alignment parameters for aged cells and the changes in full-cell capacity listed in Table 1. Fig. 8(a) shows LAM$_{an}$, which displays an increasing trend during cell cycling. As discussed above, a lower anode capacity loss is determined if the aged anode curves or anode curves calculated with the blend electrode model are used than when using the pristine anode curve, because the left-shift of the anode features in the full-cell OCV curve is obtained in part from the changes in the shape of the anode curve rather than solely from compression of the anode curve. The values obtained for LAM$_{an}$ with aged anode curves are very similar to those obtained using synthetic curves calculated with the blend electrode model. If changes in the silicon–graphite OCP are considered, the LAM$_{an}$ after 486 EFC is estimated at 13.1%. In contrast, the LAM$_{an}$ is estimated at 15.5% if the pristine silicon–graphite OCP is used. Regardless of whether or not changes in the silicon–graphite OCP are considered, the LAM$_{an}$ is identified as an important degradation mode for this cell type and under these operation conditions. Significant degradation by LAM$_{an}$ has also been reported by other authors [4,26,44] for this cell. Still, the loss of anode material is probably overestimated by something in the order of a few percentage points if no changes in the shape of the silicon–graphite OCP are considered.
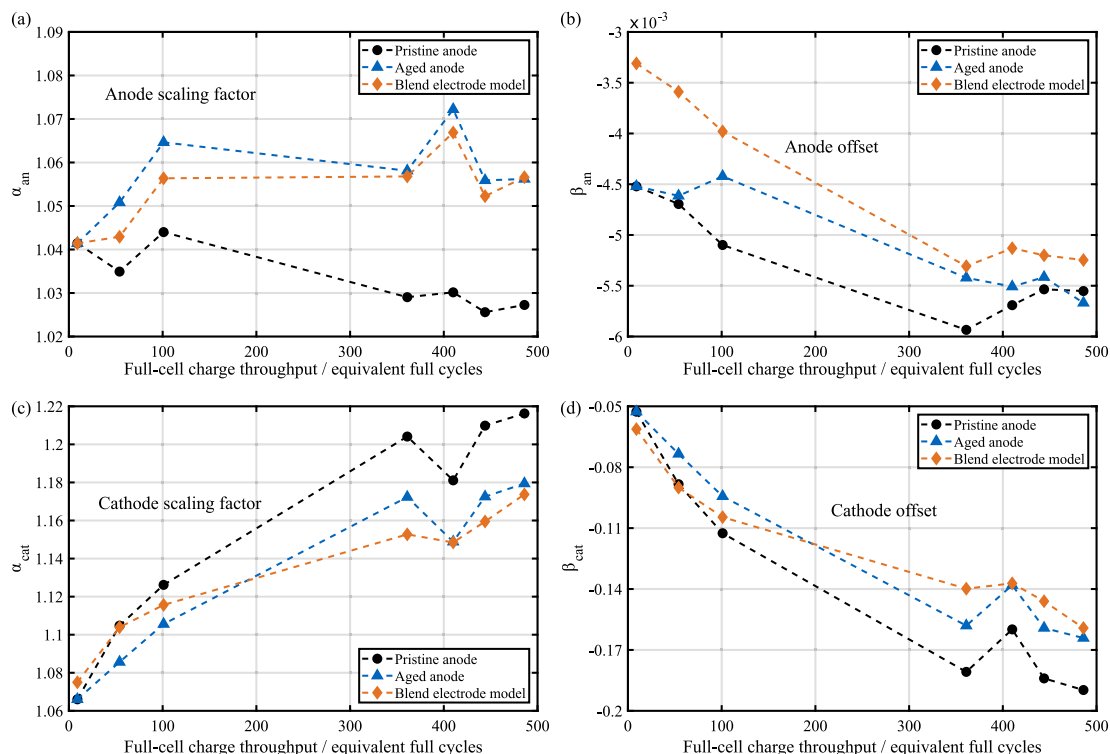
Fig. 6. Alignment parameters obtained by reconstructing the full-cell OCV curve at different aging states using different types of anode half-cell curves: (a) anode scaling factor, (b) anode offset, (c) cathode scaling factor, (d) cathode offset.
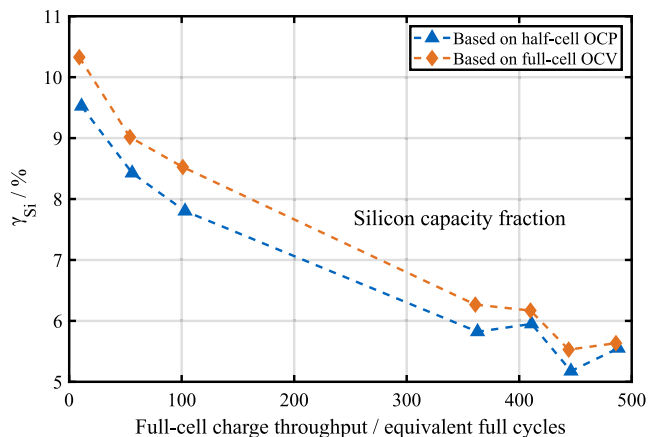

Fig. 7. Estimate of the fraction of anode capacity provided by the silicon at different aging states. Results obtained by reconstruction of half-cell OCP curves of silicon–graphite and full-cell OCV curves are shown.

LAM_{cat} during cycling is shown in Fig. 8(b). During the first 100 EFC, the estimated values for LAM_{cat} are negative, which corresponds to a slight increase in cathode capacity. The capacity increase is more pronounced if the pristine anode half-cell curve is used. After 100 EFC, LAM_{cat} starts to increase. Using aged anode curves yields similar values for the more aged cells ($\geq$361 EFC) to those obtained with the blend electrode model. Using the pristine anode curve results in values for the LAM_{cat} of cells cycled for more than 361 EFC that are approximately 3 percentage points lower. The drop in cathode capacity might therefore be slightly underestimated, when changes in the shape of the anode curve are neglected. Overall, the loss of cathode active material is much lower than LAM_{an}, which is in accordance with the literature [29,43,44], regardless of whether changes in the silicon–graphite OCP are considered or not. For example, if the measured aged

anode curves are used, 5.3 % LAM_{cat} and 15.5 % LAM_{an} are estimated for the cell cycled for 486 EFC.

Fig. 8(c) shows the LLI for different aging states. The LLI exhibits an increasing trend during cycling. The estimate for the LLI is very similar to the relative capacity loss of the cells listed in Table 1. At all aging states, the amount of available lithium in the electrodes that could be delithiated up to the upper electrode cut-off voltage is only slightly higher than the amount of lithium used within the voltage limits of the full-cell. This means that there is significant LLI throughout aging. The estimated LLI is up to 1.1 percentage points higher if changes in the silicon–graphite OCP are considered.

Summing up the results regarding the degradation modes, the capacity loss observed for this cell type under these operating conditions is caused by both LAM_{an} and LLI. Considering aging-induced changes in the shape of the anode half-cell curve leads to lower estimates for LAM_{an} and higher estimates for LAM_{cat} and LLI, and improves the validity of the estimates for the individual degradation modes.

5. Conclusion

Expanding on the results of our previous study regarding the changes in the shape of the OCP curve of silicon–graphite during full-cell cycling [22], we show that these changes in the OCP curve can be described by a blend electrode model. Fitting OCP curves of cycle-aged silicon–graphite with the model enables the capacity fraction contributed by the individual electrode components to be estimated. We deduce from the half-cell OCP measurements that the capacity fraction provided by the silicon is approximately 9.5 % for a pristine electrode decreasing to 5.5 % for an electrode cycled for 488 EFC in the full-cell configuration. The silicon therefore degrades faster than the graphite under the operating conditions used in our study.

An accurate reconstruction of aged full-cell OCV curves can be obtained by shifting and scaling half-cell OCP curves regardless of whether aging-related changes in the shape of the silicon–graphite OCP are considered or not. Still, the validity of the degradation mode
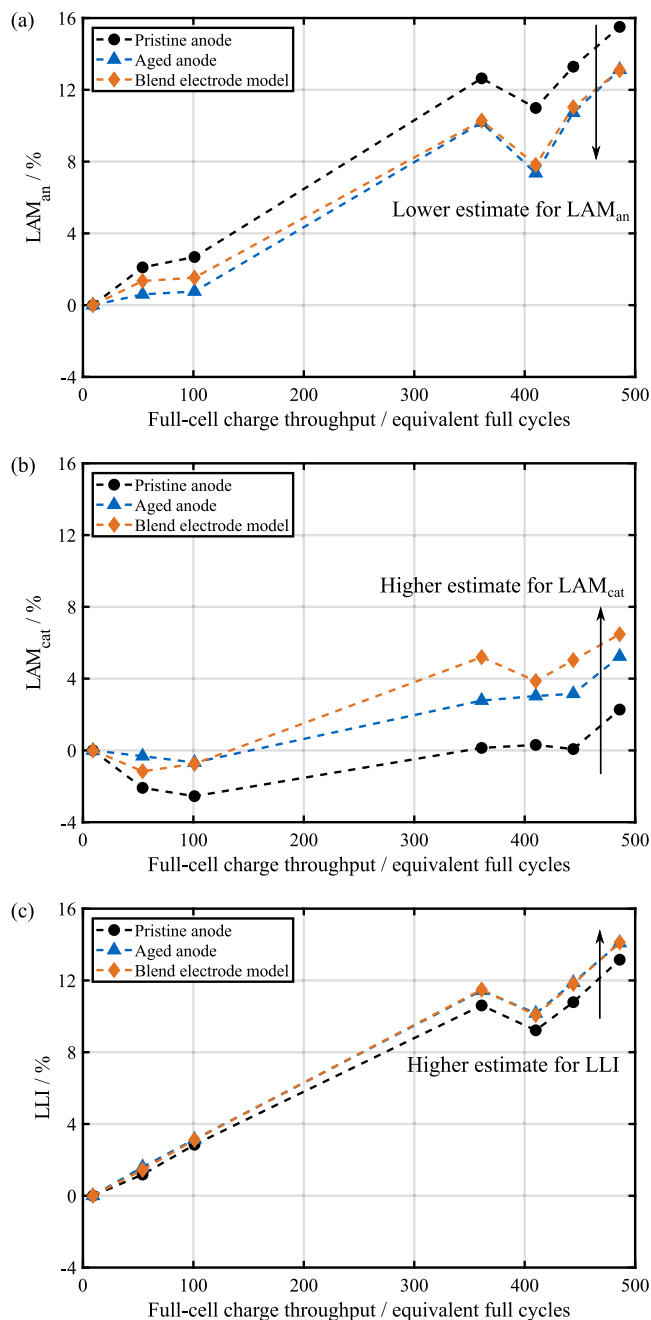
Fig. 8. (a) Loss of active material of the anode, (b) loss of active material of the cathode, and (c) loss of lithium inventory for cells cycled for a different number of equivalent full-cycles estimated via reconstruction of full-cell quasi-stationary OCV curves. The results obtained using the pristine anode half-cell curve, aged anode half-cell curves, and synthetic anode half-cell curves calculated with the blend electrode model are shown.

based on low-current full-cell charging curves are similar to those that we obtain from silicon–graphite half-cell lithiation measurements. The method proposed in this study can be used for the destruction-free estimation of the component specific degradation of silicon–graphite.

Besides analyzing low-current charging curves measured under laboratory conditions, this diagnostic method might also be applied to the analysis of cell degradation based on measurements obtained during typical charging phases of applications. Further research is necessary to investigate how the proposed method performs using only partial charging curves or charging curves obtained at higher current rates.

Table of abbreviations

CC	Constant current
CCCV	Constant current constant voltage
CT	X-ray computed tomography
CV	Constant voltage
DV	Differential voltage
EDS	Energy-dispersive X-ray spectroscopy
EFC	Equivalent full cycle
ICP-OES	Inductively coupled plasma-optical emission spectroscopy
LAM_{an}	Loss of active material of the anode
LAM_{cat}	Loss of active material of the cathode
LLI	Loss of lithium inventory
MJ1	LG Chem INR18650-MJ1 (cell type)
NMC	Lithium nickel manganese cobalt oxide
OCP	(Half-cell) open-circuit potential
OCV	(Full-cell) open-circuit voltage
RMSE	Root-mean-square error
SOC	State of charge

CRediT authorship contribution statement

Julius Schmitt: Conceptualization, Methodology, Validation, Formal analysis, Investigation, Writing – original draft, Writing – review & editing, Visualization. **Markus Schindler:** Writing – review & editing. **Andreas Oberbauer:** Investigation, Writing – review & editing. **Andreas Jossen:** Writing – review & editing, Supervision, Project administration, Funding acquisition.

Declaration of competing interest

The authors declare that they have no known competing financial interests or personal relationships that could have appeared to influence the work reported in this paper.

Appendix. Derivation of formula for silicon mass fraction

Absolute silicon capacity C_{Si} is calculated as a fraction of the total capacity of the blend C_{blend}:

$$C_{Si} = \gamma_{Si} \cdot C_{blend}. \tag{A.1}$$

Silicon capacity can also be calculated as:

$$C_{Si} = m_{Si} \cdot c_{Si}, \tag{A.2}$$

estimates obtained with this diagnostic method can be improved by considering aging-induced changes in the shape of the silicon–graphite OCP curve. For the investigated cell, the loss of anode active material is probably slightly overestimated, while the loss of cathode active material and the LLI are slightly underestimated if changes in the silicon–graphite OCP are neglected.

In addition, expanding the diagnostic method by using synthetic anode curves calculated with a blend electrode model, as proposed in this study, enables an estimation of the anode capacity fraction provided by the individual electrode components. The estimates that we obtain for the anode capacity fraction provided by the silicon

where m_{Si} is the silicon mass and c_{Si} the gravimetric specific capacity of silicon. Similarly,

$$C_G = m_G \cdot c_G \tag{A.3}$$

applies to the graphite capacity C_G, with m_G being the graphite mass and c_G the gravimetric specific capacity of graphite. The total blend capacity is defined as:

$$C_{blend} = C_{Si} + C_G, \tag{A.4}$$

and the total mass of the active blend material M_{blend} is given by:

$$M_{blend} = m_{Si} + m_G. \tag{A.5}$$

Using the equality of the right-hand sides of Eqs. (A.1) and (A.2) yields:

$$\gamma_{Si} \cdot C_{blend} = m_{Si} \cdot c_{Si}, \tag{A.6}$$

and substituting Eq. (A.4) leads to:

$$\gamma_{Si} \cdot (C_{Si} + C_G) = m_{Si} \cdot c_{Si}. \tag{A.7}$$

Substituting Eqs. (A.3) and (A.2) leads to:

$$\gamma_{Si} \cdot (m_{Si} \cdot c_{Si} + m_G \cdot c_G) = m_{Si} \cdot c_{Si}. \tag{A.8}$$

Solving Eq. (A.5) for m_G and substituting into Eq. (A.8) results in:

$$\gamma_{Si} \cdot (m_{Si} \cdot c_{Si} + (M_{blend} - m_{Si}) \cdot c_G) = m_{Si} \cdot c_{Si}, \tag{A.9}$$

which can be rearranged to Eq. (16).

References

[1] M. Schindler, J. Sturm, S. Ludwig, A. Durdel, A. Jossen, Comprehensive analysis of the aging behavior of nickel-rich, silicon-graphite lithium-ion cells subject to varying temperature and charging profiles, J. Electrochem. Soc. (2021) http://dx.doi.org/10.1149/1945-7111/ac03f6.

[2] A. Maheshwari, M. Heck, M. Santarelli, Cycle aging studies of lithium nickel manganese cobalt oxide-based batteries using electrochemical impedance spectroscopy, Electrochim. Acta 273 (2018) 335–348, http://dx.doi.org/10.1016/j.electacta.2018.04.045.

[3] J. Schmitt, B. Kraft, J.P. Schmidt, B. Meir, K. Elian, D. Ensling, G. Keser, A. Jossen, Measurement of gas pressure inside large-format prismatic lithium-ion cells during operation and cycle aging, J. Power Sources 478 (2020) 228661, http://dx.doi.org/10.1016/j.jpowsour.2020.228661.

[4] I. Zilberman, J. Sturm, A. Jossen, Reversible self-discharge and calendar aging of 18650 nickel-rich, silicon-graphite lithium-ion cells, J. Power Sources 425 (2019) 217–226, http://dx.doi.org/10.1016/j.jpowsour.2019.03.109.

[5] J. Schmitt, A. Maheshwari, M. Heck, S. Lux, M. Vetter, Impedance change and capacity fade of lithium nickel manganese cobalt oxide-based batteries during calendar aging, J. Power Sources 353 (2017) 183–194, http://dx.doi.org/10.1016/j.jpowsour.2017.03.090.

[6] P. Keil, S.F. Schuster, J. Wilhelm, J. Travi, A. Hauser, R.C. Karl, A. Jossen, Calendar aging of lithium-ion batteries, J. Electrochem. Soc. 163 (9) (2016) A1872–A1880, http://dx.doi.org/10.1149/2.0411609jes.

[7] J.S. Edge, S. O'Kane, R. Prosser, N.D. Kirkaldy, A.N. Patel, A. Hales, A. Ghosh, W. Ai, J. Chen, J. Yang, S. Li, M.-C. Pang, L. Bravo Diaz, A. Tomaszewska, M.W. Marzook, K.N. Radhakrishnan, H. Wang, Y. Patel, B. Wu, G.J. Offer, Lithium ion battery degradation: what you need to know, Phys. Chem. Chem. Phys. : PCCP 23 (14) (2021) 8200–8221, http://dx.doi.org/10.1039/d1cp00359c.

[8] M. Dubarry, C. Truchot, B.Y. Liaw, Synthesize battery degradation modes via a diagnostic and prognostic model, J. Power Sources 219 (2012) 204–216, http://dx.doi.org/10.1016/j.jpowsour.2012.07.016.

[9] J.P. Schmidt, H.Y. Tran, J. Richter, E. Ivers-Tiffée, M. Wohlfahrt-Mehrens, Analysis and prediction of the open circuit potential of lithium-ion cells, J. Power Sources 239 (2013) 696–704, http://dx.doi.org/10.1016/j.jpowsour.2012.11.101.

[10] X. Han, M. Ouyang, L. Lu, J. Li, Y. Zheng, Z. Li, A comparative study of commercial lithium ion battery cycle life in electrical vehicle: Aging mechanism identification, J. Power Sources 251 (2014) 38–54, http://dx.doi.org/10.1016/j.jpowsour.2013.11.029.

[11] K. Honkura, T. Horiba, Study of the deterioration mechanism of LiCoO2/graphite cells in charge/discharge cycles using the discharge curve analysis, J. Power Sources 264 (2014) 140–146, http://dx.doi.org/10.1016/j.jpowsour.2014.04.036.

[12] C.R. Birkl, E. McTurk, M.R. Roberts, P.G. Bruce, D.A. Howey, A parametric open circuit voltage model for lithium ion batteries, J. Electrochem. Soc. 162 (12) (2015) A2271–A2280, http://dx.doi.org/10.1149/2.0331512jes.

[13] A. Marongiu, N. Nlandi, Y. Rong, D.U. Sauer, On-board capacity estimation of lithium iron phosphate batteries by means of half-cell curves, J. Power Sources 324 (2016) 158–169, http://dx.doi.org/10.1016/j.jpowsour.2016.05.041.

[14] C.R. Birkl, M.R. Roberts, E. McTurk, P.G. Bruce, D.A. Howey, Degradation diagnostics for lithium ion cells, J. Power Sources 341 (2017) 373–386, http://dx.doi.org/10.1016/j.jpowsour.2016.12.011.

[15] C.R. Birkl, E. McTurk, S. Zekoll, F.H. Richter, M.R. Roberts, P.G. Bruce, D.A. Howey, Degradation diagnostics for commercial lithium-ion cells tested at −10°C, J. Electrochem. Soc. 164 (12) (2017) A2644–A2653, http://dx.doi.org/10.1149/2.1401712jes.

[16] S. Schindler, M.A. Danzer, A novel mechanistic modeling framework for analysis of electrode balancing and degradation modes in commercial lithium-ion cells, J. Power Sources 343 (2017) 226–236, http://dx.doi.org/10.1016/j.jpowsour.2017.01.026.

[17] Y. Gao, J. Jiang, C. Zhang, W. Zhang, Y. Jiang, Aging mechanisms under different state-of-charge ranges and the multi-indicators system of state-of-health for lithium-ion battery with Li(NiMnCo)O2 cathode, J. Power Sources 400 (2018) 641–651, http://dx.doi.org/10.1016/j.jpowsour.2018.07.018.

[18] Z. Ma, Z. Wang, R. Xiong, J. Jiang, A mechanism identification model based state-of-health diagnosis of lithium-ion batteries for energy storage applications, J. Clean. Prod. 193 (2018) 379–390, http://dx.doi.org/10.1016/j.jclepro.2018.05.074.

[19] X. Jia, C. Zhang, Y. Le Wang, L. Zhang, W. Zhang, The degradation characteristics and mechanism of Li[Ni 0.5 Co 0.2 Mn 0.3]o 2 batteries at different temperatures and discharge current rates, J. Electrochem. Soc. 167 (2) (2020) 020503, http://dx.doi.org/10.1149/1945-7111/ab61e9.

[20] S. Lee, P. Mohtat, J.B. Siegel, A.G. Stefanopoulou, J.-W. Lee, T.-K. Lee, Estimation error bound of battery electrode parameters with limited data window, IEEE Trans. Ind. Inform. 16 (5) (2020) 3376–3386, http://dx.doi.org/10.1109/TII.2019.2952066.

[21] S. Lee, J.B. Siegel, A.G. Stefanopoulou, J.-W. Lee, T.-K. Lee, Electrode state of health estimation for lithium ion batteries considering half-cell potential change due to aging, J. Electrochem. Soc. 167 (9) (2020) 090531, http://dx.doi.org/10.1149/1945-7111/ab8c83.

[22] J. Schmitt, M. Schindler, A. Jossen, Change in the half-cell open-circuit potential curves of silicon–graphite and nickel-rich lithium nickel manganese cobalt oxide during cycle aging, J. Power Sources 506 (1) (2021) 230240, http://dx.doi.org/10.1016/j.jpowsour.2021.230240.

[23] M. Klett, J.A. Gilbert, S.E. Trask, B.J. Polzin, A.N. Jansen, D.W. Dees, D.P. Abraham, Electrode behavior RE-visited: Monitoring potential windows, capacity loss, and impedance changes in Li 1.03 (Ni 0.5 Co 0.2 Mn 0.3) 0.97 O 2 /silicon-graphite full cells, J. Electrochem. Soc. 163 (6) (2016) A875–A887, http://dx.doi.org/10.1149/2.0271606jes.

[24] M. Wetjen, D. Pritzl, R. Jung, S. Solchenbach, R. Ghadimi, H.A. Gasteiger, Differentiating the degradation phenomena in silicon-graphite electrodes for lithium-ion batteries, J. Electrochem. Soc. 164 (12) (2017) A2840–A2852, http://dx.doi.org/10.1149/2.1921712jes.

[25] W.M. Dose, M.J. Piernas-Muñoz, V.A. Maroni, S.E. Trask, I. Bloom, C.S. Johnson, Capacity fade in high energy silicon-graphite electrodes for lithium-ion batteries, Chem. Commun. (Cambr. Engl.) 54 (29) (2018) 3586–3589, http://dx.doi.org/10.1039/c8cc00456k.

[26] X. Li, A.M. Colclasure, D.P. Finegan, D. Ren, Y. Shi, X. Feng, L. Cao, Y. Yang, K. Smith, Degradation mechanisms of high capacity 18650 cells containing Si-graphite anode and nickel-rich NMC cathode, Electrochim. Acta 297 (2019) 1109–1120, http://dx.doi.org/10.1016/j.electacta.2018.11.194.

[27] M. Wetjen, S. Solchenbach, D. Pritzl, J. Hou, V. Tileli, H.A. Gasteiger, Morphological changes of silicon nanoparticles and the influence of cutoff potentials in silicon-graphite electrodes, J. Electrochem. Soc. 165 (7) (2018) A1503–A1514, http://dx.doi.org/10.1149/2.1261807jes.

[28] D. Anseán, G. Baure, M. González, I. Cameán, A.B. García, M. Dubarry, Mechanistic investigation of silicon-graphite/LiNi0.8Mn0.1Co0.1O2 commercial cells for non-intrusive diagnosis and prognosis, J. Power Sources 459 (2020) 227882, http://dx.doi.org/10.1016/j.jpowsour.2020.227882.

[29] T.M.M. Heenan, A. Jnawali, M.D.R. Kok, T.G. Tranter, C. Tan, A. Dimitrijevic, R. Jervis, D.J.L. Brett, P.R. Shearing, An advanced microstructural and electrochemical datasheet on 18650 Li-ion batteries with nickel-rich NMC811 cathodes and graphite-silicon anodes, J. Electrochem. Soc. 167 (14) (2020) 140530, http://dx.doi.org/10.1149/1945-7111/abc4c1.

[30] H. Popp, N. Zhang, M. Jahn, M. Arrinda, S. Ritz, M. Faber, D.U. Sauer, P. Azais, I. Cendoya, Ante-mortem analysis, electrical, thermal, and ageing testing of state-of-the-art cylindrical lithium-ion cells, E I Elektrotech. Inform. 137 (4–5) (2020) 169–176, http://dx.doi.org/10.1007/s00502-020-00814-9.

[31] J. Sturm, A. Rheinfeld, I. Zilberman, F.B. Spingler, S. Kosch, F. Frie, A. Jossen, Modeling and simulation of inhomogeneities in a 18650 nickel-rich, silicon-graphite lithium-ion cell during fast charging, J. Power Sources 412 (2019) 204–223, http://dx.doi.org/10.1016/j.jpowsour.2018.11.043.

[32] M. Schindler, J. Sturm, S. Ludwig, J. Schmitt, A. Jossen, Evolution of initial cell-to-cell variations during a three-year production cycle, ETransportation 14 (165) (2021) 100102, http://dx.doi.org/10.1016/j.etran.2020.100102.

[33] I. Zilberman, S. Ludwig, A. Jossen, Cell-to-cell variation of calendar aging and reversible self-discharge in 18650 nickel-rich, silicon–graphite lithium-ion cells, J. Energy Storage 26 (2019) 100900, http://dx.doi.org/10.1016/j.est.2019.100900.

[34] E. Moyassari, L. Streck, N. Paul, M. Trunk, R. Neagu, C.C. Chang, S.-C. Hou, B. Märkisch, R. Gilles, A. Jossen, Impact of silicon content within silicon-graphite anodes on performance and li concentration profiles of li-ion cells using neutron depth profiling, J. Electrochem. Soc. (2021) http://dx.doi.org/10.1149/1945-7111/abe1db.

[35] R. Jung, R. Morasch, P. Karayaylali, K. Phillips, F. Maglia, C. Stinner, Y. Shao-Horn, H.A. Gasteiger, Effect of ambient storage on the degradation of Ni-rich positive electrode materials (NMC811) for Li-ion batteries, J. Electrochem. Soc. 165 (2) (2018) A132–A141, http://dx.doi.org/10.1149/2.0401802jes.

[36] F. Friedrich, B. Strehle, A.T.S. Freiberg, K. Kleiner, S.J. Day, C. Erk, M. Piana, H.A. Gasteiger, Editors' choice—Capacity fading mechanisms of NCM-811 cathodes in lithium-ion batteries studied by X-ray diffraction and other diagnostics, J. Electrochem. Soc. 166 (15) (2019) A3760–A3774, http://dx.doi.org/10.1149/2.0821915jes.

[37] R. Jung, M. Metzger, F. Maglia, C. Stinner, H.A. Gasteiger, Oxygen release and its effect on the cycling stability of LiNi x Mn y Co z O 2 (NMC) cathode materials for li-ion batteries, J. Electrochem. Soc. 164 (7) (2017) A1361–A1377, http://dx.doi.org/10.1149/2.0021707jes.

[38] J. Li, J.R. Dahn, An in situ X-Ray diffraction study of the reaction of li with crystalline Si, Electrochem. Solid-State Lett. 154 (3) (2007) A156, http://dx.doi.org/10.1149/1.2409862.

[39] I. Zilberman, S. Ludwig, M. Schiller, A. Jossen, Online aging determination in lithium-ion battery module with forced temperature gradient, J. Energy Storage 28 (2020) 101170, http://dx.doi.org/10.1016/j.est.2019.101170.

[40] Y. Nishi, Lithium ion secondary batteries; past 10 years and the future, J. Power Sources 100 (1–2) (2001) 101–106, http://dx.doi.org/10.1016/S0378-7753(01)00887-4.

[41] S. Schweidler, L. de Biasi, A. Schiele, P. Hartmann, T. Brezesinski, J. Janek, Volume changes of graphite anodes revisited: A combined operando X-ray diffraction and in situ pressure analysis study, J. Phys. Chem. C 122 (16) (2018) 8829–8835, http://dx.doi.org/10.1021/acs.jpcc.8b01873.

[42] J. Sieg, M. Storch, J. Fath, A. Nuhic, J. Bandlow, B. Spier, D.U. Sauer, Local degradation and differential voltage analysis of aged lithium-ion pouch cells, J. Energy Storage 30 (2020) 101582, http://dx.doi.org/10.1016/j.est.2020.101582.

[43] E. Coron, S. Geniès, M. Cugnet, P.X. Thivel, Impact of lithium-ion cell condition on its second life viability, J. Electrochem. Soc. 167 (11) (2020) 110556, http://dx.doi.org/10.1149/1945-7111/aba703.

[44] E. Coron, S. Geniès, M. Cugnet, P.X. Thivel, High-energy li-ion cells: Impact of electrode ageing on second life viability, J. Electrochem. Soc. 168 (10) (2021) 100539, http://dx.doi.org/10.1149/1945-7111/ac3112.